Atomic Reconstruction and Oxygen Evolution

Reaction of Mn₃O₄ Nanoparticles

4   Sangmoon Yoon[†,‡], Hongmin Seo[†], Kyoungsuk Jin[†,§], Hyoung Gyun Kim[†], Seung-Yong Lee[†,¶],

5   Janghyun Jo[†], Kang Hee Cho[†], Jinseok Ryu[†], Aram Yoon[ǁ], Young-Woon Kim[†], Jian-Min Zuo[ǁ],

6   Young-Kyun Kwon[±], Ki Tae Nam[†], and Miyoung Kim[†,*]

7   [†] Department of Materials Science and Engineering, Seoul National University, Seoul 08826,

8   Republic of Korea

9   [‡] Department of Physics, Gachon University, Seongnam, Gyeonggi-do 13120, Republic of Korea

10   [§] Department of Chemistry and Research Institute for Natural Sciences, Korea University, Seoul

11   02841, Republic of Korea

12   [¶] Division of Materials Science and Engineering, Hanyang University, Seoul 04763, Republic of

13   Korea

14   [ǁ] Department of Materials Science and Engineering, University of Illinois, Urbana-Champaign,

15   Illinois 61801, United States

16   [±] Department of Physics, Department of Information Display, and Research Institute for Basic

17   Sciences, Kyung Hee University, Seoul 02447, Republic of Korea

18

19   EXPERIMETNAL/COMPUTATIONAL METHODS

20   *Synthesis of Mn₃O₄ nanoparticles*

21 To prepare the Mn_3O_4 nanoparticles, monodispersed MnO nanoparticles were first prepared by a

22 modified hot injection method. MnO nanoparticles were converted to Mn_3O_4 nanoparticles by

23 annealing under an air atmosphere with the temperature and time of 150 °C and 1 hour,

24 respectively. The ligands attached on the surfaces of as-prepared MnO nanoparticles were removed

25 during annealing. Note that the ligand removal procedures via heat treatment or ligand exchange

26 are essential for activation of OER because the organic ligand obstructs the access of water

27 molecules on the nanoparticle surface. The Mn_3O_4 phase was identified by both X-ray diffraction

28 (XRD) and selective area electron diffraction (SAED), as shown in Figure S9 and Figure 2(a),

29 respectively.

30 *Electrochemical measurements*

31 Electrochemical experiments were conducted using a three-electrode electrochemical cell system.

32 A BASi Ag/AgCl/3M NaCl reference electrode and Pt foil (2 cm × 2 cm × 0.1 mm, 99.997%

33 purity; Alfa Aesar, Ward Hill, MA) were used as the reference electrode and counter electrode,

34 respectively. The working Mn_3O_4-nanoparticle electrodes were fabricated as follows. First, as-

35 prepared MnO nanoparticles were spin-coated on fluorine-doped tin oxide (FTO)-coated glass

36 with surface resistivity of 15 Ω sq^{-1}. The spin-coating step was conducted at a spin rate of 2,000

37 rpm and a holding time of 10 s. The spin-coated film on the FTO substrates was then annealed at

38 150°C for 1 hour to make the final Mn_3O_4-nanoparticle electrode. Electrochemical tests were

39 carried out at ambient temperature (21°C ± 1°C) using a potentiostat system (CH Instruments,

40 Austin, TX). The electrode potential was converted to the normal hydrogen electrode (NHE) scale

41 using the following equation: E(NHE) = E(Ag/AgCl) + 0.18 V. The electrolyte was phosphate

42 buffer with 500 mM buffer strength at pH 7.0. Prior to each electrochemical test, the electrolyte

43 resistance was measured. All cyclic voltammetry (CV) curves were IR-compensated and

44 polarization-corrected to remove the contribution of the non-faradaic current.

45 *STEM/EELS measurements*

46 STEM/EELS measurements were performed on an aberration-corrected JEOL-ARM 200CF,

47 operating at 200 kV, installed at the National Center for Inter-university Research Facilities

48 (NCIRF), Seoul National University. The microscope is equipped with a cold-field-emission type

49 gun and a 964 GIF Quantum ER EELS detector. For STEM imaging, a sub-angstrom electron

50   probe with a convergence semiangle of 19 mrad was used. The collection inner and outer

51   semiangles for HAADF STEM were 68 and 280 mrad, respectively. For EELS measurements, a

52   sub-nanometer electron probe with a convergence angle of 13 mrad and larger current was used,

53   and the collection semiangle was 63 mrad. The energy dispersion was set at 0.25 eV per channel.

54   The full-width at half-maximum of the zero-loss peak in a vacuum was 1.0 eV. Scan noise arising

55   in the high-resolution STEM images was reduced by band-pass filtering. To minimize the electron-

56   irradiation damage during EELS spectrum imaging, EELS spectra were measured at 30 frames per

57   second. TEM sample was prepared by dispersing MnO nanoparticles on a lacey carbon grid and

58   then annealing them directly. The ultra-small nanoparticles exhibit higher OER activity, but the

59   15 nm-sized particles were investigated in this work as larger nanoparticles were less sensitive to

60   the damages induced by the electron beam. The environmental TEM experiments were carried out

61   using Hitachi H-9500 dynamic TEM with K2 IS camera for direct electron detection.

62   *Ab initio DFT calculations*

63   *Ab initio* DFT calculations were performed using the Vienna *ab initio* simulation package

64   (VASP) code. The Perdew–Burke–Ernzerhof plus Hubbard correction (PBE + U + J) was used for

65   the exchange-correlation functional, in which the double-counting interactions were corrected

66   using the full localized limit (FLL). The values used for the on-site direct Coulomb parameter (U)

67   and the anisotropic Coulomb parameter (J) were 4.0 and 1.2 eV, respectively. A plane wave basis

68   set at a cutoff energy of 500 eV was used to expand the electronic wave functions, and the valence

69   electrons were described using the projector-augmented wave potentials. The Γ-centered $3 \times 3 \times$

70   1 Monkhorst-Pack K-point grid was used for sampling the Brillouin zone. The collinear

71   ferrimagnetic configuration was considered in this study, where Mn^{2+} spins were

72   ferromagnetically aligned and all Mn^{3+} spins were antiferromagnetically aligned. Lim *et al*.

73   showed that this ferrimagnetic order is the lowest-energy magnetic structure in DFT + U + J

74   calculations. To model the Mn_3O_4 surfaces, a symmetric slab model with a vacuum region larger

75   than 15 Å was used. All atoms were relaxed by the conjugate gradient algorithms until none of the

76   remaining Hellmann–Feynman forces acting on any atoms exceeded 0.02 eV Å^{-1}.

77   SUPPLEMENTARY FIGURES
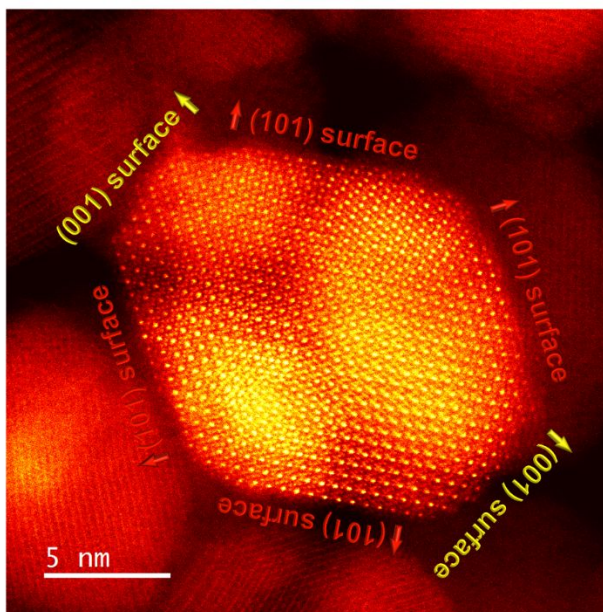
78

79   **Figure S1.** High-resolution HAADF STEM image of a nanoparticle viewed along the [100] zone

80   axis. Surface profile images viewed along the [100] zone axis allows the (010), (001), and (101)

81   surface to be examined. This profile image indicates that Mn_3O_4 nanoparticles could have (001)

82   facets in addition to the (110) and (101) facets observed in other profile images viewed along the

83   [111] zone axis.
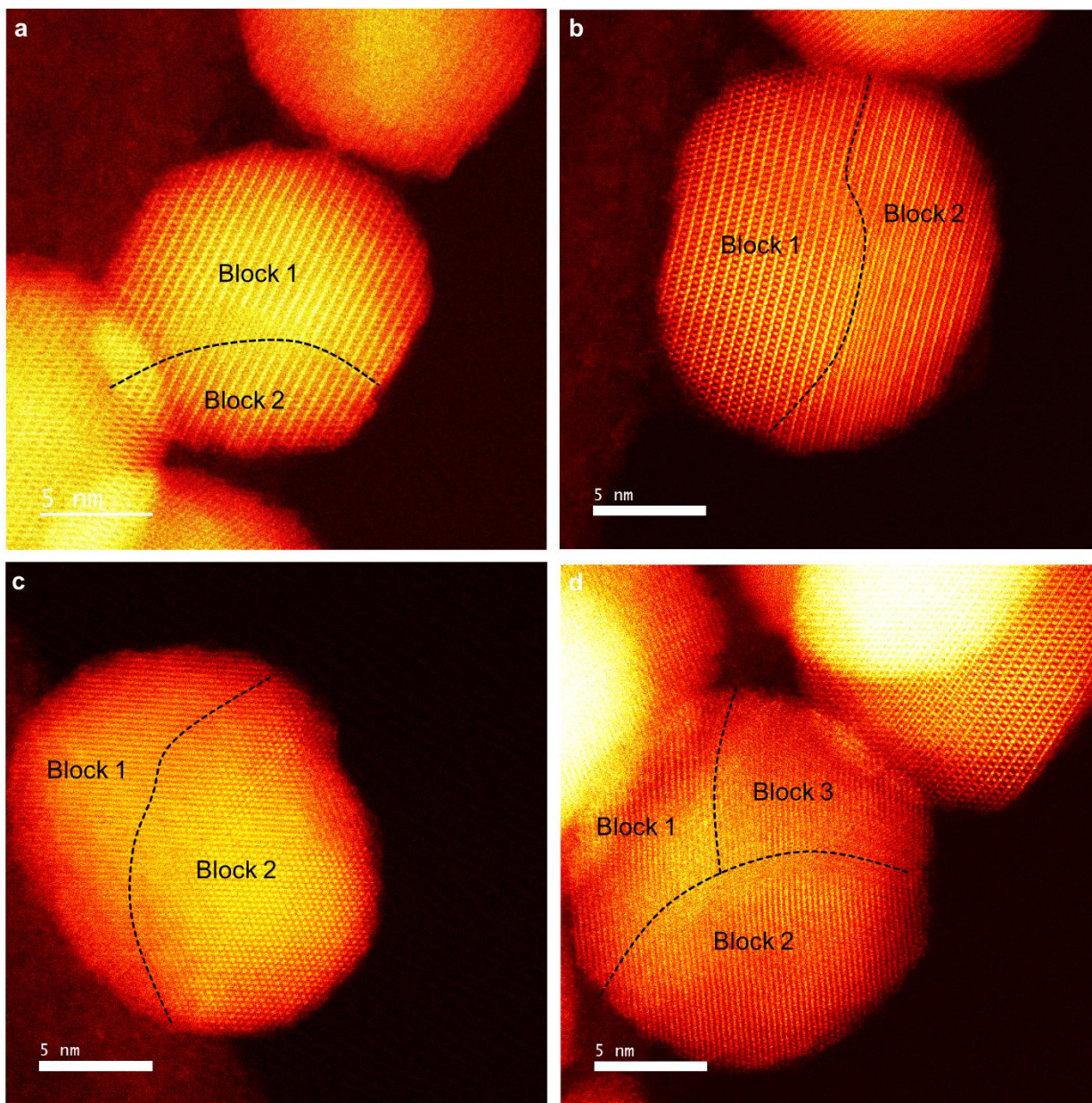
84   **Figure S2.** Atomic structure of multi-mosaic Mn_3O_4 nanoparticles. (a)–(d) High-resolution

85   HAADF STEM images of Mn_3O_4 nanoparticles composed of multi-mosaic blocks. Note that the

86   nanoparticles are still surrounded by (101), (110), and (001) facets despite the multigrain structure.

88
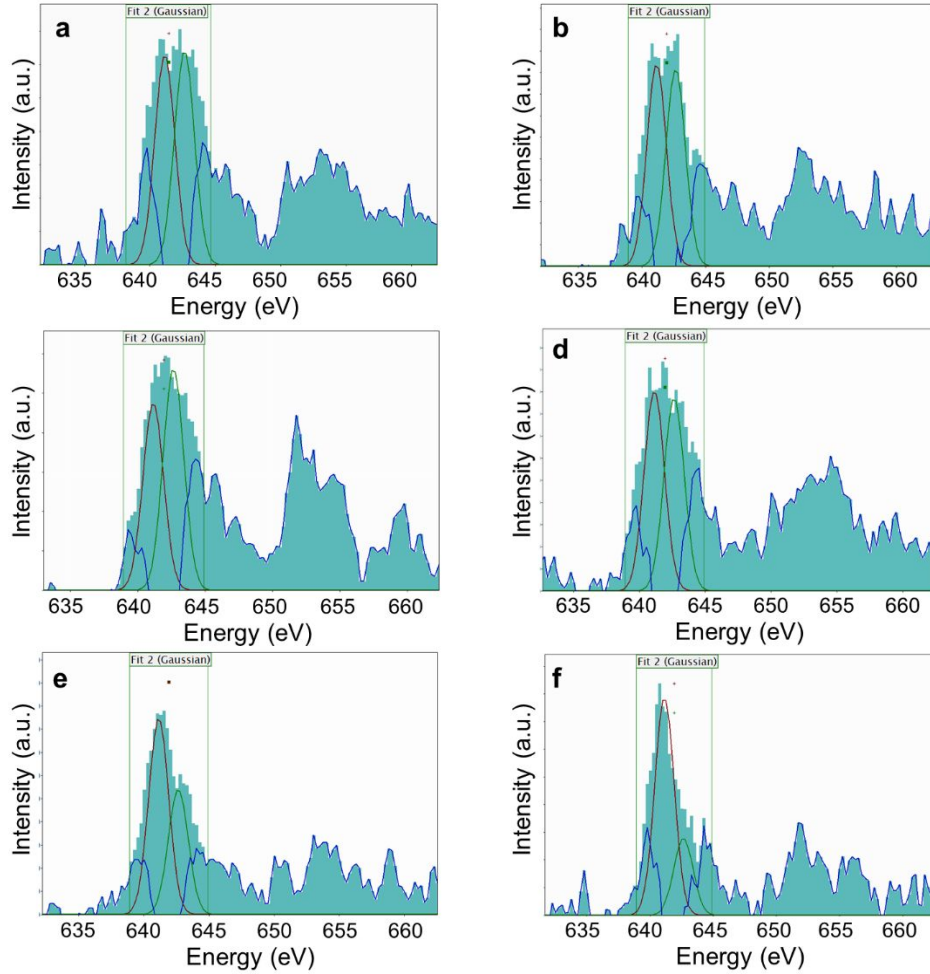
Figure S3. Two Gaussian fitting of Mn L_3 edge to analyze the intensity ratio of Mn^{2+} and Mn^{3+}

90 (I^{3+}/I^{2+}) in Mn_3O_4 nanoparticles. (a)–(d) Raw spectra inside the nanoparticle and (e)–(f) those at

91 the nanoparticle surface. According to the references, the L_3 peaks of Mn^{2+} and Mn^{3+} appear at

92 641.0 and 642.5 eV, respectively. Here, we used the Gaussian functions to estimate the spectral

93 weight of Mn^{2+} and Mn^{3+} peak intensities. The L_3 edge of each spectrum is fitted with the two

94 Gaussian functions centered at 641.0 (brown solid line) and 642.5 eV (green solid line). With

95 regard to the spectral weight, the former Gaussian function and the latter one correspond to the

96 Mn^{2+} and Mn^{3+} peaks, respectively. The blue solid lines denote the residual signal remained after

97   the two gaussian fitting. This intensity ratio of two Gaussian functions, I^{3+}/I^{2+}, is displayed as a

98   color map in Figure 3d. Note that the intensity ratio of the surface spectra (e)–(f) is smaller than

99   that of the bulk spectra (a)–(d). The mean and standard deviation of the intensity ratio at the inner

100   region, surface and edge of the nanoparticle were 0.96 ± 0.18, 0.45 ± 0.14, and 0.91 ± 0.06,

101   respectively.
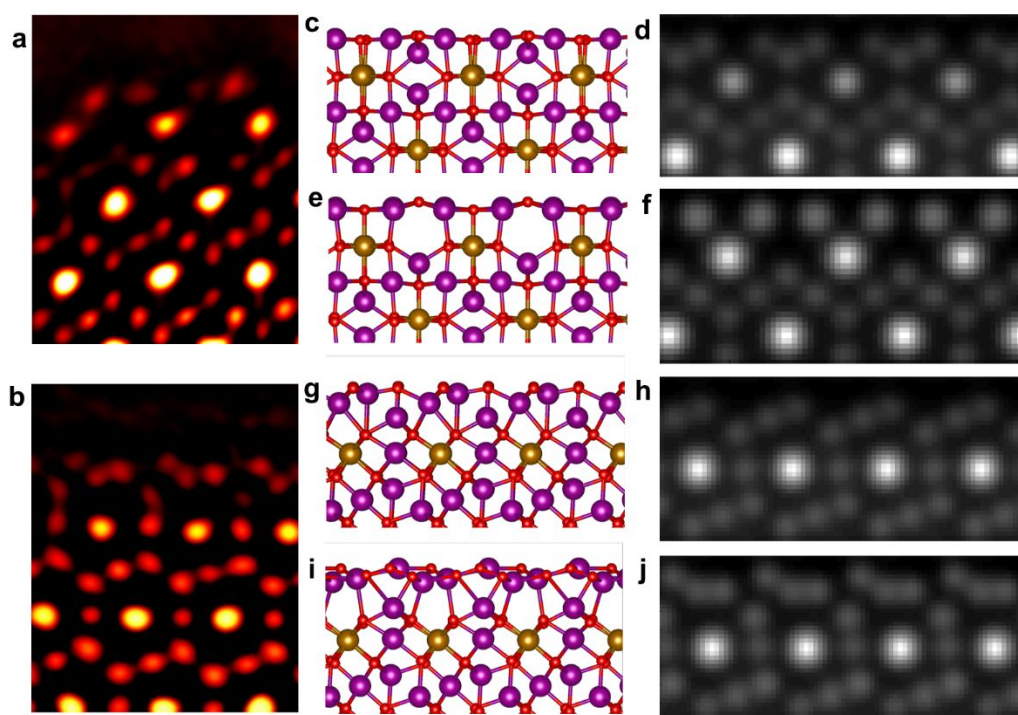
102

103   **Figure S4.** Verification of atomic surface models via multislice HAADF STEM simulations. (a),(b)

104   Enlarged HAADF STEM images of the (110) and (101) surfaces, respectively. Atomic structure

105   model and simulated STEM image of the (110) surface: (c)–(d) cleaved surface and (e)–(f)

106   reconstructed surface. Atomic structure model and simulated STEM image of the (101) surface:

S7

107   (g)–(h) cleaved surface and (i)–(j) reconstructed surface. Simulated HAADF STEM images from

108   the reconstructed surface models show good agreement with the experimental HAADF STEM

109   images.
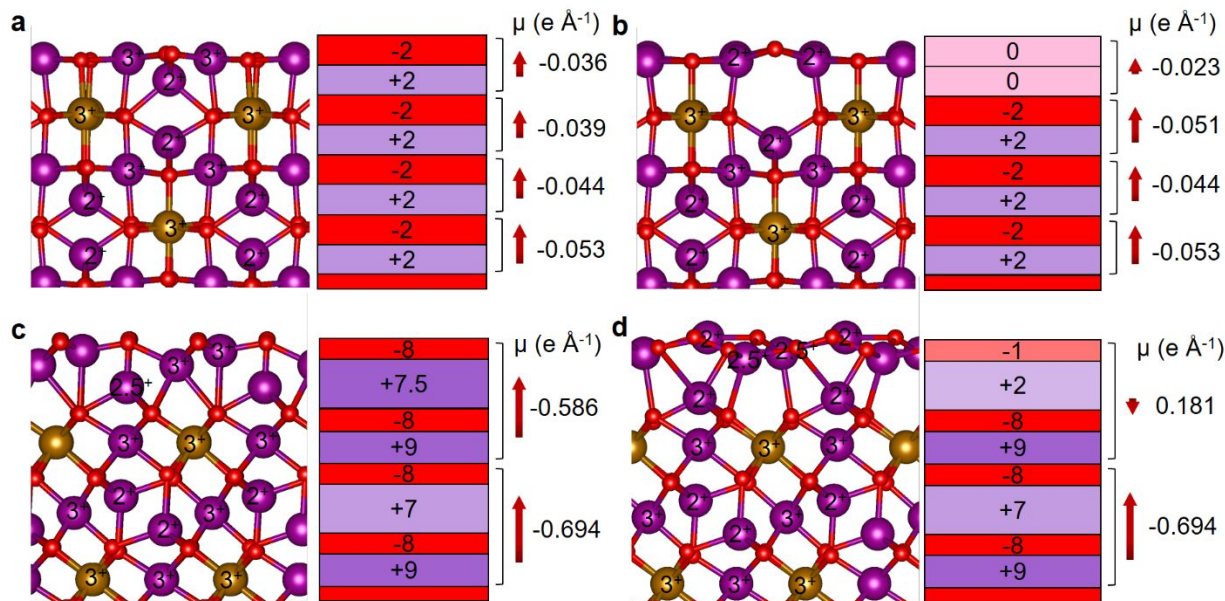
110

111   **Figure S5.** Compensation of surface polarity in the (110) and (101) reconstructed surface. Atomic

112   surface models, schematics for atomic charged layers, and corresponding surface polarization: (a)

113   (110) cleaved surface, (b) (110) reconstructed surface, (c) (101) cleaved surface, and (d) (011)

114   reconstructed surface. The charge of each atomic layer is estimated based on numerically derived

115   oxidation state (see Table 1). The surface polarization is estimated by $\vec{\mu} = \sum_i (q_i \cdot z_i / A)\hat{n}$, where

116   i denotes the ionic site in the repeated unit perpendicular to the surface and A is the surface area

117   of the corresponding structural unit. q_i and z_i refer to the charge of the ith ion and the atomic

118   coordinate in the direction perpendicular to the surface, respectively. For the (110) surface, the

119   polarity of the top surface is fully neutralized by the surface reconstruction. For the (101) surface,
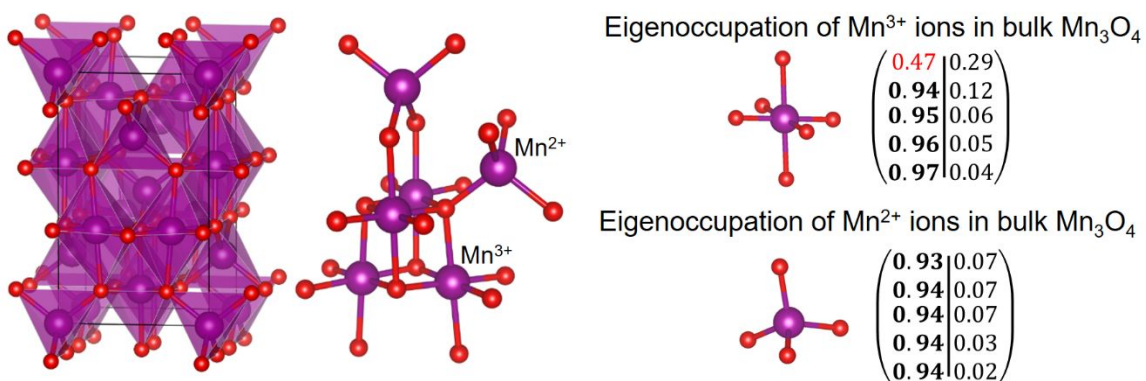
120   the polarity of the top-surface layer become weaker as additional Mn^{2+} ions are embedded into the

121   uppermost osxygen layer. It verifies that the atomic rearrangement observed in STEM images

122   compensates the surface polarity on both the (110) and (101) surfaces.
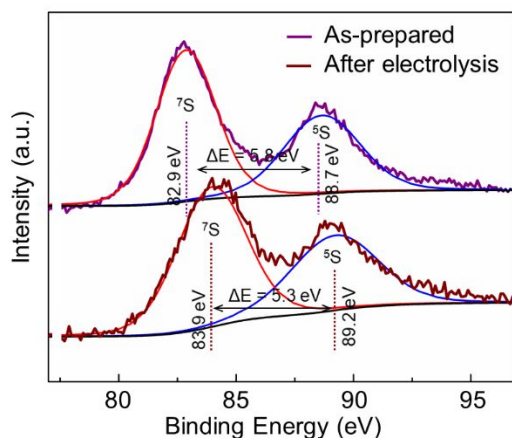

123

124   **Figure S6.** X-ray photoemission spectroscopy (XPS) Mn 3s spectra of Mn_3O_4 nanoparticles before

125   and after OER. The after-electrolysis XPS spectrum was measured after applying a constant

126   current density of 1 mA/cm^2 for 30 minutes. The change of peak split (ΔE) between ^7S and ^5S

127   peaks reflects the modification of surface electronic state through the continuous chemical

128   reactions. Absorption of surface ligands may have affected the XPS spectrum. The ratio of low-

129   index facets to edge may have been changed during the reaction. The surface atomic configurations

130   could have been modified during the OER. For *in-detail* understanding of the corresponding

131   change, further *in-situ* or *ex-situ* STEM/EELS works are required. For reference, Mn_3O_4 have the

132   peak split in the range of 5.3eV to 5.8eV.[1-4]

133

Eigenoccupation of Mn^{3+} ions in bulk Mn_3O_4

$$\begin{pmatrix} 0.47 & 0.29 \\ 0.94 & 0.12 \\ 0.95 & 0.06 \\ 0.96 & 0.05 \\ 0.97 & 0.04 \end{pmatrix}$$

Eigenoccupation of Mn^{2+} ions in bulk Mn_3O_4

$$\begin{pmatrix} 0.93 & 0.07 \\ 0.94 & 0.07 \\ 0.94 & 0.07 \\ 0.94 & 0.03 \\ 0.94 & 0.02 \end{pmatrix}$$

134

135 **Figure S7.** Orbital occupation (i.e. eigenoccupation) of Mn^{3+} and Mn^{2+} states in bulk Mn_3O_4. Mn

136 ions in octahedral and tetrahedral sites at bulk phase are in the Mn^{3+} and Mn^{2+} states, respectively.

137 Eigenoccupation (f_{Mn}) of Mn^{3+} and Mn^{2+} ions in the bulk is summarized on the right side. The left

138 and right columns in the f_{Mn} indicate the orbital occupations of majority and minority spins,

139 respectively. The occupied, unoccupied, and partially unoccupied orbitals are denoted in black

140 boldface, red, and blue, respectively. Note that ~0.5 electron is still occupied in the unoccupied

141 (majority-spin) orbital of Mn^{3+} ions because of the hybridization with O ions. In other words, the

142 (majority-spin) orbital with ~0.5 electron can be considered as an unoccupied orbital in the analysis

143 of eigenoccupation. Mn 1 and 4 in the (110) and (101) cleaved surfaces have identical orbital states

144 with the Mn^{3+} ions in bulk Mn_3O_4.

145
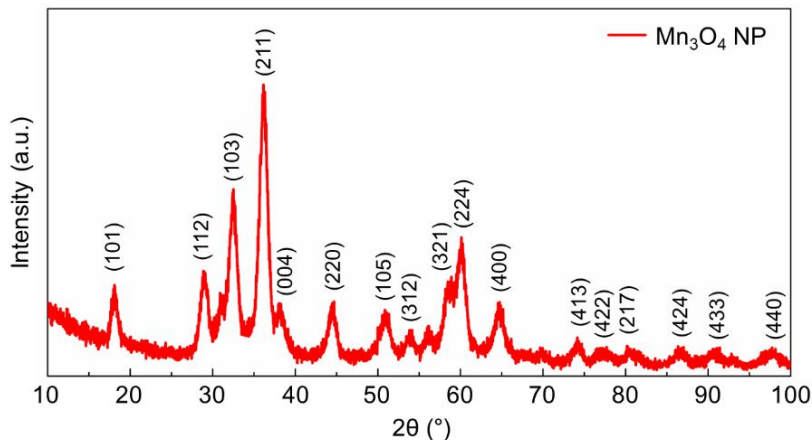
146 **Figure S8.** X-ray diffraction (XRD) pattern of Mn_3O_4 nanoparticles. The XRD peaks were indexed

147 based on the crystallographic data of the tetragonal spinel Mn_3O_4 (Hausmannite, JCPDS-24-0734).

148 **Reference**

149 1.   Gorlin, Y.; Lassalle-Kaiser, B.; Benck, J. D.; Gul, S.; Webb, S. M.; Yachandra, V. K.;
150 Yano, J.; Jaramillo, T. F., In situ X-ray absorption spectroscopy investigation of a bifunctional
151 manganese oxide catalyst with high activity for electrochemical water oxidation and oxygen
152 reduction. *Journal of the American Chemical Society* **2013,** *135* (23), 8525-8534.
153 2.   Nelson, A.; Reynolds, J. G.; Roos, J. W., Core-level satellites and outer core-level
154 multiplet splitting in Mn model compounds. *Journal of Vacuum Science & Technology A:*
155 *Vacuum, Surfaces, and Films* **2000,** *18* (4), 1072-1076.
156 3.   Dhanalaxmi, K.; Singuru, R.; Kundu, S. K.; Reddy, B. M.; Bhaumik, A.; Mondal, J.,
157 Strongly coupled Mn 3 O 4–porous organic polymer hybrid: a robust, durable and potential
158 nanocatalyst for alcohol oxidation reactions. *RSC advances* **2016,** *6* (43), 36728-36735.
159 4.   Lin, R.; Zhu, Z.; Yu, X.; Zhong, Y.; Wang, Z.; Tan, S.; Zhao, C.; Mai, W., Facile
160 synthesis of TiO 2/Mn 3 O 4 hierarchical structures for fiber-shaped flexible asymmetric
161 supercapacitors with ultrahigh stability and tailorable performance. *Journal of Materials*
162 *Chemistry A* **2017,** *5* (2), 814-821.

163

164